

by

G. Volpe and M. J. Siclari  
Grumman Corporate Research Center  
Bethpage, New York 11714-3580

and

A. Jameson  
Department of Mechanical and Aerospace Engineering  
Princeton University  
Princeton, New Jersey 08544

*A87-49052*

Abstract

An algorithm for computing transonic flow fields about fighter-type aircraft is described in the paper. The compressible Euler equations are solved numerically using a vertex-based, finite volume multigrid scheme. The space around the aircraft is discretized with a single-block H-O mesh which is generated by the union of separate O-meshes around successive cross sections of the aircraft. The discretized equations are integrated via a five-stage Runge-Kutta scheme, and a variety of techniques -- local time-step maximization, residual smoothing and enthalpy damping -- are used along with a multigrid scheme to accelerate convergence to the steady state. The algorithm has proved to be very efficient in practice, and several examples at transonic and supersonic free stream conditions are presented.

Introduction

The ability to compute the flow field about an aircraft is of paramount importance to the airplane designer. Accuracy and speed are the qualities of a computer code which determine the extent of its usefulness. Accuracy is required to reduce uncertainties, of course. Speed of execution determines the number of different configurations and/or flow conditions that can be investigated in a given time span (and with a given computing machine). More extensive investigations lead to a more refined design, usually. Methods based on the full potential equation<sup>1-4</sup> have been, and are still being, widely used in airplane design. However, because of the inherent theoretical assumptions, the accuracy of such methods deteriorates when large regions of rotational flow (e.g., strong shocks, separation) are present in the flow field. The Navier-Stokes equations provide a more accurate model of the flow field, and several codes<sup>5-7</sup> are available for their solution. However, they require large amounts of storage and long running times. As a result, their use in airplane design is, at present, limited. In addition, they are not entirely reliable because of the uncertainties in the current status of turbulence models. By assuming inviscid flow and thus reducing the Navier-Stokes equations to the Euler equations, we can skirt the turbulence-modeling problem, but we obtain a more accurate representation of the flow field than the one offered by the velocity potential assumption. Over the last few years, several methods<sup>8-18</sup> have been developed for the solution of the Euler equations

in both two-dimensional and three-dimensional flow. In general, they require substantially more computer memory storage than their full-potential counterparts, but such requirements are within the capabilities of present-day machines. The running times of three-dimensional Euler codes must be reduced, however, if they are to be used routinely in airplane design. In this paper a new multigrid finite volume method for the solution of the Euler equations is presented. The numerical scheme is very efficient and enables the calculation of aircraft flow fields to be performed in 5-10 min of computing time on a Cray-XMP class machine for both transonic and supersonic free stream conditions.

The basis of the method is the integration of the time-dependent Euler equations until they reach a steady state. The integration is performed using a Runge-Kutta scheme on a set of discretized equations. These are obtained by first dividing the flow field into hexahedral cells and then writing the conservation laws in integral form for each cell. Space discretization is accomplished with a single-block H-O grid which we found to be well suited to low aspect ratio aircraft configuration. Such a grid is obtained by the union of two-dimensional meshes generated in planes normal to the longitudinal axis of the aircraft. Each 2-D mesh is obtained by mapping the local cross section of the wing-body configuration into a near circle. A polar-like coordinate grid in the transformed corresponds to a grid in the physical plane that not only has a good concentration of points in regions of high curvature but is also body-conforming. This is a highly desirable feature since it simplifies the application of boundary conditions. Planes can be spaced at will in the longitudinal direction. The resulting 3-D grid is of the O-type if viewed in the normal planes, and of the H-type if viewed in planes parallel to the longitudinal axis.

The compressible Euler equations are discretized by requiring conservation of mass, momentum, and energy in each cell of the mesh, and these are integrated by a finite-volume scheme originally due to Jameson (Ref 19). The scheme is second-order accurate (except in the vicinity of shock waves) and is very efficient. Dissipative terms, which vanish in the limit of zero cell volume, are added to the discretized equations in order to suppress odd-even point decoupling and oscillations near shock waves. The equations are integrated with a five-stage Runge-Kutta scheme. Very high values of the Courant number can be used by making the time step vary locally and by smoothing of the residuals. Additional accelera-

tion is provided by enthalpy damping, and, finally, a multigrid sequencing of the meshes is invoked to turn this interactive integration scheme into a very rapid method for reaching the steady state.

### Mesh Generation

The three-dimensional mesh around a fighter-type aircraft configuration is obtained by generating two-dimensional meshes around pre-selected cross sections of the aircraft in planes normal to the longitudinal axis of the aircraft. Upstream and downstream of the aircraft, the mesh is a continuation of the first and last stations on the aircraft, respectively. The scheme was originally suggested by Moretti<sup>20</sup> and has been used by Siclari<sup>21</sup> in the computation of supersonic full potential flows by space marching techniques.

An arbitrary cross section may consist of the fuselage body alone, the wing and body, or even the wing alone with or without an intervening slit between it and the plane of symmetry. Each of these cross sections  $Z = X + iY$  is mapped into a near circle by removing sequentially all singularities (corners) of the cross-section via a Karman-Trefftz mapping of the type

$$\left(\frac{Z - Z_0}{Z + \bar{Z}_0}\right) = \left(\frac{\zeta - Z_0}{\zeta + \bar{Z}_0}\right)^\tau \quad (1)$$

where  $\zeta$  denotes the ordinate in the mapped plane and  $Z_0$  the location of the singularity (with  $Z$  the conjugate value).  $\tau\pi$  is the external angle of the corner to be removed. Equation (1) is applied as many times as there are singularities. On mappings subsequent to the first,  $Z$  and  $\tau$  in Eq (1) are to be interpreted as the values in the most recently mapped plane. Once all the corners are removed, the cross section is a near-circle in the final mapped plane, and a polar-like coordinate grid can be generated around the body in a straightforward manner. Grid lines wrapping around the body are gradually distorted into a perfect circle at a predetermined distance denoting the outer boundary of the mesh. Radial grid lines emanating from a point equidistant from the vertical and horizontal extremes of the mapped cross section will then give the second family of lines for the mesh. Since the mapped cross section is a near circle, the mesh will usually automatically provide adequate clustering near wing tips. Additional clustering in the azimuthal direction, as well as in the radial direction, can be obtained by the use of stretching functions.

The distance to which the 2-D mesh in each plane extends is kept constant. Upstream of the aircraft's nose, the 3-D grid is generated by extending the first mesh plane of the aircraft upstream to a pre-determined distance with a gradually increasing spacing between planes. Since the aircraft nose eventually comes to a point, all the points around a cross-section degenerate into a single point at the nose. The grid will therefore contain a degenerate axis upstream of the aircraft, a topological feature that requires attention in the solution of the discretized equations. The grid past the last station on the aircraft is similarly extended downstream of the last 2-D mesh on the aircraft. This last mesh usually wraps

around a slit since the last cross-section typically includes the wing's trailing edge and/or the wake.

A representative grid is shown in Fig. 1-3. Typically one-half of the planes are stationed

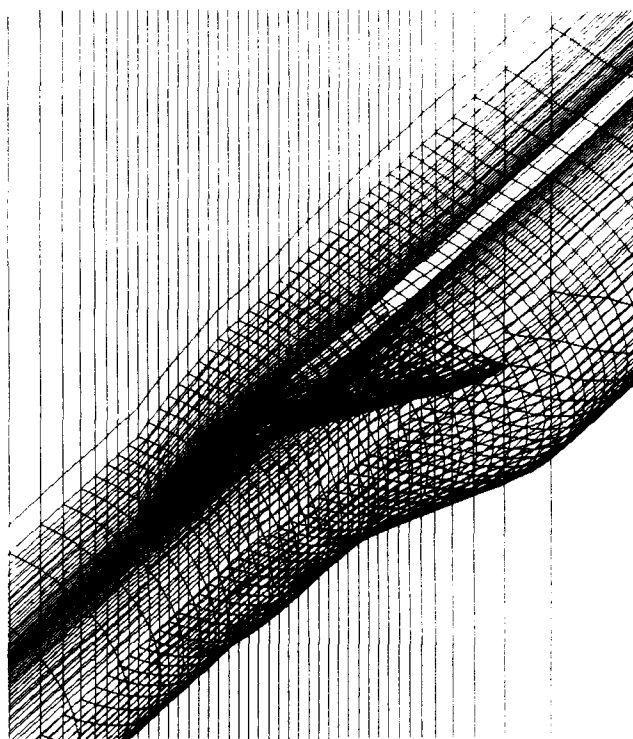


Fig. 1 Grid Lines in Symmetry Plane, on Wing/Fuselage/Wake Surface and on a Shell Around the Aircraft

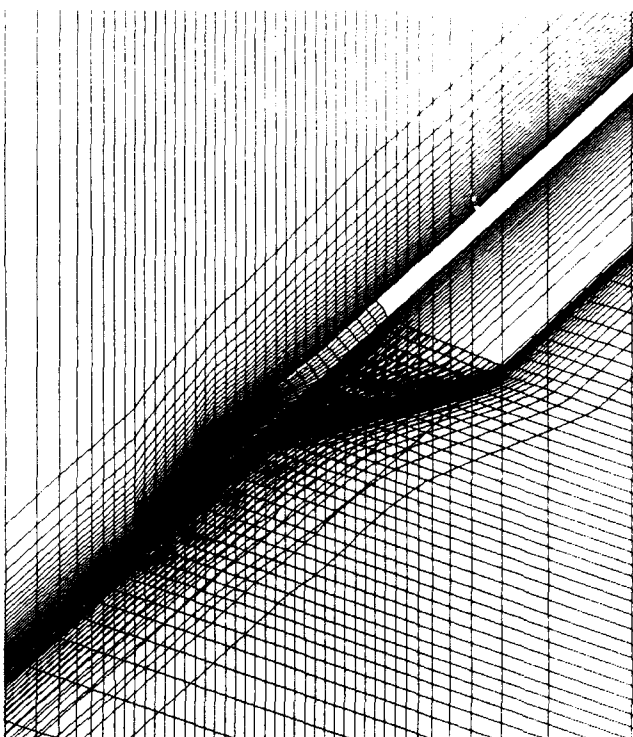
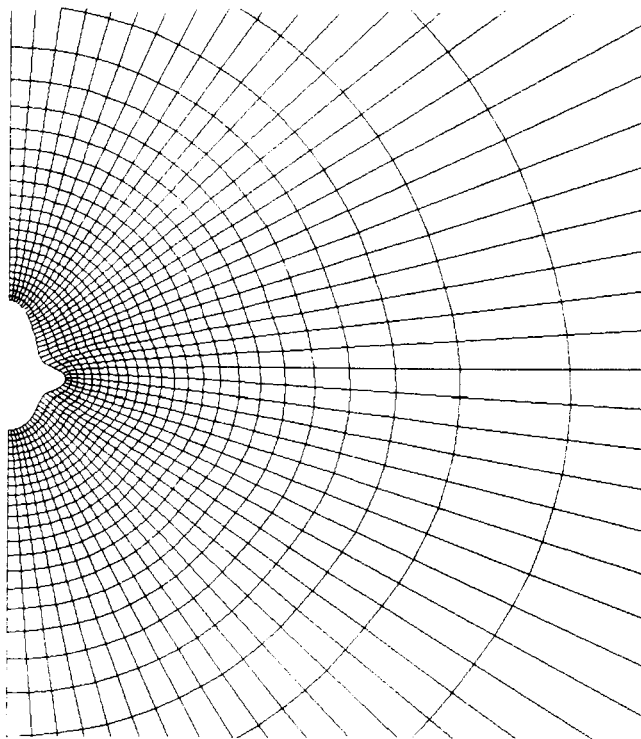
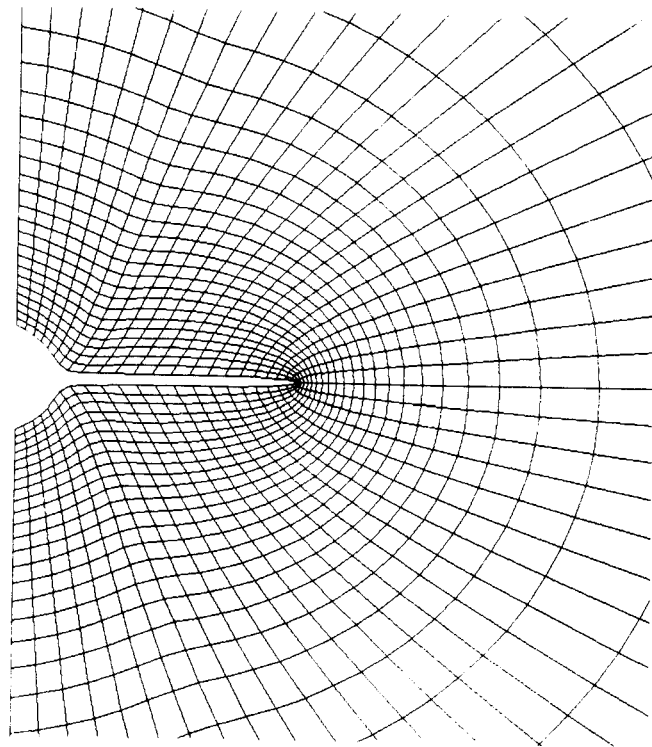


Fig. 2 Grid Line in Symmetry Plane, on Wing/Fuselage/Wake Surface and in Longitudinal Plane Touching the Wing Tip



a) Plane Through Front Fuselage



b) Plane Through Wing

Fig. 3 Grid Lines in Cross-sectional Planes

between the nose and the tail of the aircraft, one quarter upstream, and one quarter downstream. Figure 1 depicts the grid in the symmetry plane, along with the surface grid and a grid surface wrapping around the body. Figure 2 shows a surface running along the aircraft, and Fig. 3a,b depicts the grid in two typical cross-sectional planes.

A variation to this strategy that makes more efficient use of grid points in cases when the free stream is supersonic, is to vary the distance to which the 2-D mesh in each cross-sectional plane extends. This distance can be kept small near the aircraft's nose and be increased downstream until it reaches a maximum value. In addition, with restricted domains of dependence and influence, more grid planes can be concentrated along the aircraft's body. A typical grid which can be used in cases where the free stream Mach number is supersonic is depicted in Fig. 4. In this grid, which contains as many total points as the one shown in Fig. 1-3, two-thirds of the planes are concentrated on the aircraft.

#### Finite-Volume Discretization

The conservation laws for mass, momentum, and energy over a three-dimensional domain  $\Omega$  enclosed by a surface boundary  $\partial\Omega$  are expressed by the following integral form of the Euler equations:

$$\frac{\partial}{\partial t} \iiint_{\Omega} w^{(i)} d\Omega + \iint_{\partial\Omega} \vec{F}^{(i)} \cdot d\vec{S} = 0 \quad (2)$$

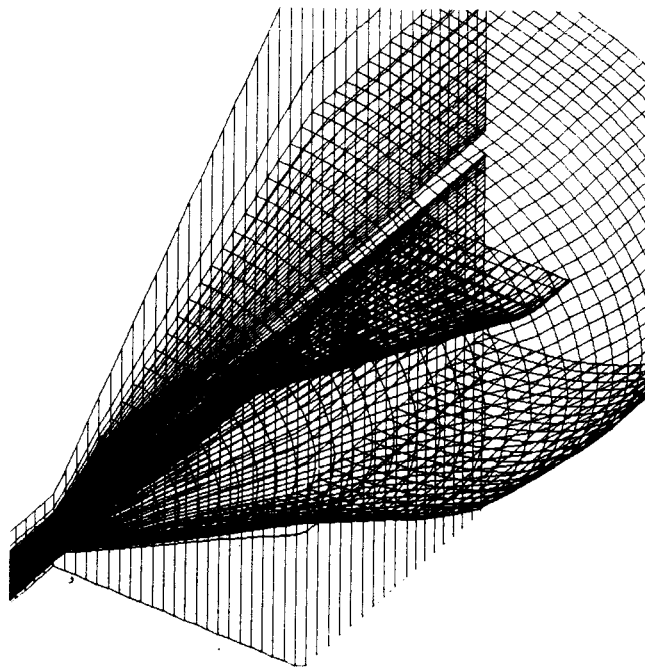


Fig. 4 Grid Lines in Symmetry Plane, on Wing/Fuselage/Wake Surface and on a Shell Around the Aircraft for a Supersonic Free Stream

where  $W^{(i)}$  is a conserved quantity and  $\bar{F}^{(i)}$  is its corresponding flux term. The first term then is simply the rate of change over time in the quantity, and the second is the total flux into (out of) the domain. For mass conservation

$$W^{(1)} = \rho, \quad \bar{F}^{(1)} = [\rho u, \rho v, \rho w]^T; \quad (3a)$$

for momentum conservation

$$W^{(2)} = \rho u, \quad \bar{F}^{(2)} = [\rho u^2 + p, \rho uv, \rho uw]^T, \quad (3b)$$

$$W^{(3)} = \rho v, \quad \bar{F}^{(3)} = [\rho uv, \rho v^2 + p, \rho vw]^T, \quad (3c)$$

$$W^{(4)} = \rho w, \quad \bar{F}^{(4)} = [\rho uw, \rho vw, \rho w^2 + p]^T; \quad (3d)$$

and for energy conservation

$$W^{(5)} = \rho E, \quad \bar{F}^{(5)} = [\rho Hu, \rho Hv, \rho Hw]^T. \quad (3e)$$

In the expressions above,  $p, \rho, u, v, w, E$  and  $H$  are, respectively, the pressure, density, Cartesian velocity components, total energy, and total enthalpy. For a perfect gas, whose ratio of specific heats is  $\gamma$ , we have the additional relations

$$E = \frac{p}{(\gamma-1)\rho} + \frac{1}{2}(u^2 + v^2 + w^2), \quad (4a)$$

$$H = E + \frac{p}{\rho}. \quad (4b)$$

Equation (2) can, of course, be applied to any subdomain  $\Omega_n$  of  $\Omega$ . Thus, by dividing the entire domain  $\Omega$  into a large number of hexahedral cells and using Eq (2) to estimate the rate of change of  $W^{(i)}$  in each subdomain, we obtain discrete approximations of the conservation laws expressed in Eq (2) over the entire domain. In the present work, the dependent flow variables  $W^{(i)}$  are assumed to be stored at the nodes of the mesh, in contrast to previous finite volume schemes in which the flow variables were stored at the cell centers. This leads to revised time stepping and multigrid formulations which have proved particularly efficient in practice. The control volume for each node  $(i, j, k)$  is given by the union of the eight cells meeting at that node. Applying Eq (2) to each of the eight cells, then, for the control volume enclosing the  $(i, j, k)$  node, one obtains

$$\frac{d}{dt} \left( \sum_{n=1}^8 V_n \right) W_n^{(i)} + \sum_{n=1}^8 Q_n^{(i)} = 0 \quad (5)$$

where the summation sign runs over the eight cells meeting at  $\{i, j, k\}$ ,  $V_n$  is the volume of the  $n$ th cell and  $Q_n^{(i)}$  is the flux balance for that cell.  $Q_n^{(i)}$  is approximated by

$$Q_n^{(i)} = \sum_{\ell} \bar{F}_{\ell}^{(i)} \cdot \bar{S}_{\ell} \quad (6)$$

where  $S_{\ell}$  is the directed face area of the  $\ell$ th face (of the  $n$ th cell) and  $\bar{F}_{\ell}^{(i)}$  is an estimate of the mean flux vector across that face. Since the fluxes across internal faces cancel, contributions to the flux balance through the control volume are given only by its external faces, as one would expect.

Background dissipation must be added over the entire domain to prevent the appearance of odd and even point oscillations which would give a net contribution of zero to the flux balance in each interior cell. Such a mode might be suppressed in the steady state solution by the boundary conditions, but the convergence rate can be adversely affected if transient oscillations are not adequately damped. Dissipation is also needed to eliminate oscillations near shock waves and contact discontinuities. Several nonoscillatory schemes for scalar conservation laws have been designed in the past few years using the concept of total variation diminishing (TVD) difference schemes introduced by Harten,<sup>22</sup> and the ideas have been extended to the treatment of the Euler equations by splitting the flux into components based on the characteristic speeds and by applying the TVD construction separately to each component. Flux splitting allows the construction of terms which introduce just enough dissipation to prevent oscillations. This in turn permits the clear capture of shock spread out over only one or two cells. An alternative approach, which is followed here, is the use of adaptive coefficients for the dissipation terms. In practice, this has been shown to work extremely well. The approach is to use a low background level everywhere in the domain and increase it in the neighborhood of a shock wave. It has been found that the second difference of the pressure provides an effective measure for detecting locations where the additional dissipation is needed.

The scheme is implemented by substituting for  $Q_n^{(i)}$  in Eq (5) a term  $Q_n^{(i)} - D_n^{(i)}$  where  $D_n^{(i)}$  is a dissipative flux constructed in such a way as to preserve the conservation form of the equations.  $D_n^{(i)}$  is the sum of three dissipation terms constructed for each of the three coordinate directions. Thus, at a node  $(i, j, k)$  the dissipation term in the  $i$  (or  $x$ ) direction is given by

$$D_n^{(i)} = d_{i+1,j,k} - d_{i,j,k} \quad (7)$$

where

$$d_{i,j,k} = r[\epsilon^{(2)} - \epsilon^{(4)} \delta_x^2] (W_{i,j,k}^{(i)} - W_{i-1,j,k}^{(i)}) \quad (8)$$

and  $\delta_x^2$  is a second difference central operator.

In Eq (8)  $\epsilon^{(2)}$  and  $\epsilon^{(4)}$  are adaptive coefficients and  $r$  is a scaling factor proportional to an estimate of the maximum local wave speed. In

an explicit scheme such as the one we use, a measure of the time it takes for the fastest wave to cross a mesh interval is given by the local time step  $\Delta t^*$ . Thus,  $r$  can be made proportional to  $1/\Delta t^*$ .  $\epsilon^{(4)}$  provides the background dissipation, which is of third order in smooth regions of the flow.  $\epsilon^{(2)}$  controls the dissipation near shock waves and is made proportional to a normalized second difference of the pressure

$$\epsilon^{(2)} \propto v_{i,j,k} = \frac{|p_{i+1,j,k} - 2p_{i,j,k} + p_{i-1,j,k}|}{p_{i+1,j,k} + 2p_{i,j,k} + p_{i-1,j,k}}$$

This part of the dissipation is thus of third order everywhere except near regions of steep pressure gradients. Dissipation terms in the  $j$  (or  $y$ ) and  $k$  (or  $z$ ) directions are constructed in a similar manner.

The low-order dissipative terms effectively introduce upwind biasing. Instead of blending low- and high-order dissipative terms, one may produce a nonoscillatory scheme by eliminating the low-order terms entirely and introducing flux limiters into the high-order terms.<sup>23</sup> This approach leads to a class of TVD schemes.

#### Time Stepping

Since we are working with a mesh that is independent of time, Eq (5) can be re-written in the form

$$\frac{d}{dt} W_{i,j,k}^{(i)} + R(W^{(i)}) = 0 \quad (9)$$

where the residual  $R(W^{(i)})$  is given by

$$R(W^{(i)}) = \frac{1}{V_{i,j,k}} (Q_{i,j,k} - D_{i,j,k}) \quad (10)$$

Here,  $V_{ijk}$ ,  $Q_{ijk}$ ,  $D_{ijk}$  are, respectively, the value of the control volume, the total flux, and the total dissipative flux through the control volume. The steady state solution is obtained by integrating Eq (9) using a five-stage Runge-Kutta scheme with a locally varying time step  $\Delta t$ . This scheme has been selected for its stability and damping properties rather than its accuracy in tracking the transient solution, since the objective is the attainment of a steady state as rapidly as possible. The stability properties of the class of multi-stage schemes to which the present scheme belongs are discussed in detail by Jameson.<sup>24</sup>

Using the superscript notation now to denote a particular stage of the time step, the advance of each variable  $W$  from time  $t$  to time  $(t + \Delta t)$  is given by

$$W^{(0)} = W(t) \quad (11a)$$

$$W^{(1)} = W(t) - \alpha_1 \Delta t R(W^{(0)}) \quad (11b)$$

$$W^{(2)} = W(t) - \alpha_2 \Delta t R(W^{(1)}) \quad (11c)$$

$$W^{(3)} = W(t) - \alpha_3 \Delta t R(W^{(2)}) \quad (11d)$$

$$W^{(4)} = W(t) - \alpha_4 \Delta t R(W^{(3)}) \quad (11e)$$

$$W^{(5)} = W(t) - \Delta t R(W^{(4)}) \quad (11f)$$

$$W(t + \Delta t) = W^{(5)} \quad (11g)$$

with  $\alpha_1 = \frac{1}{4}$ ,  $\alpha_2 = \frac{1}{6}$ ,  $\alpha_3 = \frac{3}{8}$ ,  $\alpha_4 = \frac{1}{2}$ . In practice it has been possible to freeze the artificial dissipation terms at the values computed at the second stage, a strategy which noticeably reduces the computational effort and also increases the stability margin for the dissipative terms (Ref 23).

Computational efficiency is greatly increased by smoothing the residuals. The stability limit on the local Courant number sets restrictions on the maximum permissible time step. As discussed in Ref 10, smoothing of the residuals increases the support of the numerical scheme, thus relaxing the restriction on the time step. Thus, at each point the residual is replaced by an average of its neighbors. This average is computed implicitly by solving

$$(1 - \epsilon_x \delta_x^2)(1 - \epsilon_y \delta_y^2)(1 - \epsilon_z \delta_z^2) \bar{R} = R \quad (12)$$

where  $\delta_x^2$ ,  $\delta_y^2$ ,  $\delta_z^2$  are second difference operators, and  $\epsilon_x$ ,  $\epsilon_y$ , and  $\epsilon_z$  are smoothing coefficients.

For a one-dimensional problem, and in the absence of dissipation, it can be shown (see Ref 24) that stability can be maintained for any Courant number  $\lambda$  if the smoothing parameter is chosen in such a way that

$$\epsilon \geq \frac{1}{4} \left[ \left( \frac{\lambda}{\lambda^*} \right)^2 - 1 \right]$$

where  $\lambda^*$  denotes the stability limit in the unsmoothed scheme. In practice it has been found that the fastest rate of convergence is usually obtained by setting  $\lambda$  to about three times the value of  $\lambda^*$  and using the smallest possible values of the smoothing parameters which still maintain stability.

Another useful device for accelerating convergence is enthalpy damping. Assuming that the flow is homoenthalpic, we can assume the time rate of change of each dependent variable  $W$  to be proportional to the difference between the local value of the enthalpy and its (constant) value at infinity, which is also its steady state value. Thus, we set

$$\frac{\partial W}{\partial t} + \beta W(H - H_\infty) = 0 \quad (13)$$

where  $\beta$  is a user-defined constant. We can apply this implicitly at the end of each time step through the use of

$$W = \tilde{W} + \beta \Delta t W(\tilde{H} - H_\infty) = 0 \quad (14)$$

where  $\tilde{W}$  denotes the value of  $W$  computed at the end of the time step and  $W$  is the new, improved estimate. Equation (13) is applied for each dependent variable, with only a slight modification for  $(\rho E)$ . For this last variable Eq (14) is modified to the form

$$(\rho E) - (\tilde{\rho E}) + \beta \Delta t [\rho E + \tilde{p} - \tilde{\rho H}_\infty] = 0 \quad (15)$$

### Multigrid Scheme

The objective of the multigrid scheme is to transfer part of the effort of tracking the evolution of a system of discrete equations to a sequence of successively coarser meshes. On the coarser grids, the use of larger control volumes permits the tracking of the evolution on larger scales. With the Runge-Kutta time-stepping scheme this is made possible by the use of larger time steps on the coarser grids without violating the stability bounds. An additional benefit of performing some of the time steps on coarser grids is the fact that the computational effort required is greatly reduced on the coarser meshes. This more than offsets the cost of passing information up and down through the grids.

In the present scheme the coarser meshes are generated by eliminating alternate points in each coordinate direction. This simplifies the task of transferring information through the several mesh levels. On passing from grid level  $k$  to a coarser grid level  $k+1$ , the first step of the Runge-Kutta operation described by Eq (11a) is modified to

$$W_{k+1}^{(0)} = T_{k+1,k} W_k \quad (16)$$

where  $T_{k+1,k}$  denotes a transfer operator. Since each point on the coarser mesh coincides with a point on the finer mesh, the transfer rule implied by Eq (16) is simply to assign to  $W_{k+1}^{(0)}$  the value on the coincident point in mesh level  $k$ . The subsequent steps of the Runge-Kutta operation are driven by a modified residual

$$W_{k+1}^{(1)} = W_{k+1}^{(0)} - \alpha_1 \Delta t (R_{k+1}^{(0)} + P_{k+1}) \quad (17a)$$

$$W_{k+1}^{(2)} = W_{k+1}^{(0)} - \alpha_2 \Delta t (R_{k+1}^{(1)} + P_{k+1}) \quad (17b)$$

and so on. In Eq (17)  $R_{k+1}$  is the residual computed on the mesh  $k+1$ , and

$$P_{k+1} = Q_{k+1,k} R_k(W_k) - R_{k+1}^{(0)} \quad (18)$$

where  $Q_{k+1,k}$  is another transfer operator. In the present scheme  $Q_{k+1,k} R_k(W_k)$  is a weighted average of the residuals at the 27 points nearest the coincident point on mesh level  $k$  (including the point itself).

Typically, one time step is performed on each mesh level until the coarsest (desired) mesh is reached. At this point, the end result of the Runge-Kutta step

$$W_{k+1}(t + \Delta t) = W_{k+1}^{(5)} \quad (19)$$

is transferred back to grid level  $k$  to provide an improved value. Thus, denoting by  $W_k^+$  the value of  $W_k$  resulting from both the  $k+1$  correction calculated by Eq (19) at the end of the time step and any correction transferred from a still coarser grid  $k+2$ , the value of  $W$  at grid level  $k$  is set to

$$W_k^+ = W_k + I_{k,k+1}(W_{k+1}^+ - W_{k+1}^{(0)})$$

where  $I_{k,k+1}$  is some interpolation operator. At points that are coincident on mesh levels  $k$  and  $k+1$ , the value of  $W$  is simply transferred. At intermediate points the correction is obtained by tri-linear interpolation. Usually, a V-cycle, in which correction data are transferred up through the meshes without invoking a time-integration step, is performed. Occasionally better convergence rates have been obtained with a W-cycle, in which time steps are performed on each of the meshes on the way up.

### Boundary Conditions

Configurations are assumed to be symmetric about a vertical plane in the longitudinal direction and the yaw angle is assumed to be zero. Thus, symmetry-type boundary conditions are imposed along one face of the computational cube. Flow tangency is enforced at node points lying on the aircraft, and continuity is enforced on the slit in the mesh past the wing. These boundary conditions are enforced during each stage of the Runge-Kutta time step. At the same time the value of all flow variables at each node on the degenerate axis ahead of the aircraft is replaced by the average of the values computed for the nodes sharing a common point. In the far field appropriate inflow or outflow boundary conditions are imposed using Riemann invariants to attenuate the spurious reflection of outgoing waves into the field. A more complete presentation of far field boundary conditions is contained in Ref 10.

### Numerical Examples

Results are presented here for two aircraft configurations at both transonic and low supersonic speeds. Both configurations are analytical models intended to illustrate the range of applicability of the numerical method. All cases that will be shown were run on a mesh containing 49 longitudinal planes, each containing 49 points in the azimuthal direction and 16 points in the radial direction. Since we are assuming that the flow is symmetric about the midplane (symmetry plane) of the aircraft, the mesh (as the computation) covers only one half of the configuration. A mesh of this size requires approximately 3.5 million 64-bit words of memory. All cases were run on a Cray X-MP-14 machine and the computations were performed entirely within the memory of the machine. An SSD

version of the code is under development. The numerical scheme has exhibited remarkable speed and robustness. Usually the maximum feasible number of grid levels was used in the multigrid cycle. Convergence rates, defined as the average reduction of the density residual per cycle, are typically in the 0.90-0.95 range except in cases where the angle of attack is large (greater than 10 deg) or the Mach number is supersonic; in the latter cases the convergence rate is close to 0.96. However, even in such cases, with such rates force and pressure coefficients are usually converged in fewer than 200 cycles. Fewer than 100 cycles are usually necessary for less extreme flow conditions. On the Cray X-MP-14 each multigrid cycle requires approximately 3.1 sec of CPU time for the 49x49x25 mesh. Thus, approximately 10 min were needed to compute even the hardest cases that will be shown.

The first example in Fig. 5 shows surface pressure distribution in several cross-sectional planes of the first aircraft model for a free stream Mach number of 0.95 and an angle of attack of 5°. In Fig. 5 cross-sectional cuts through the fuselage and wing are shown along with the pressure coefficient. This configuration has a canopy in the front of the fuselage, a highly-swept wing

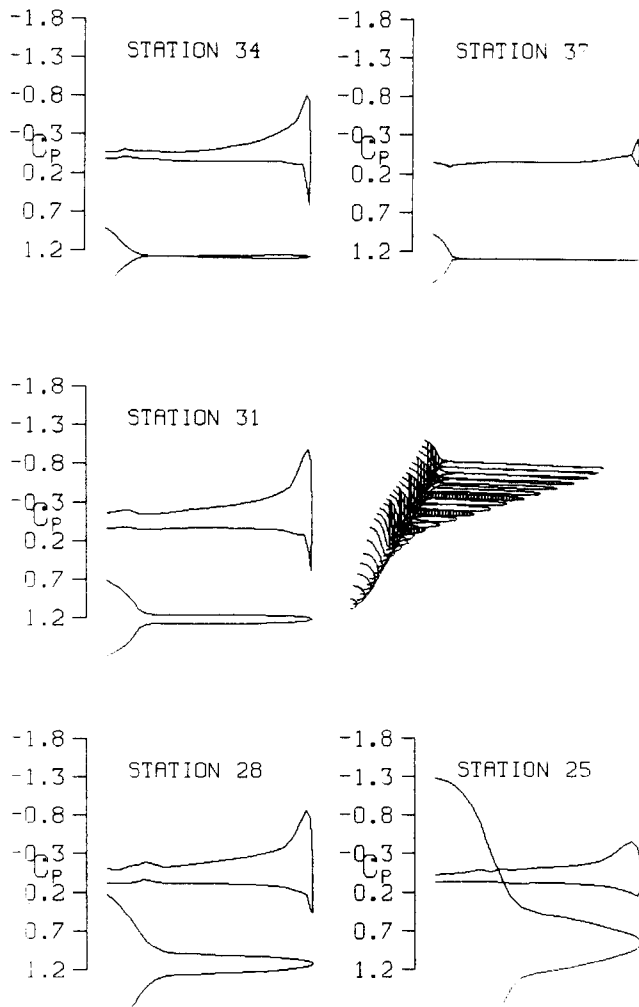


Fig. 5 Computed Surface Pressure Distributions; Configuration 1;  $M_\infty = 0.950$ ,  $\alpha = 5^\circ$

leading edge and an aft-swept trailing edge with a much reduced sweep angle. Shown in Fig. 5 are a station just past the canopy (Station 25), past the wing-joinment (Station 28), on the wing (31). Station 34 is the location at which the trailing edge of the wing leaves the fuselage. The cut at Station 36 includes part of the wake that is now present between the outer part of the wing and the rear fuselage. The aircraft's planform is seen more clearly in Fig. 6, which depicts isomach contours on the surface and in a cross-sectional plane in the rear of the configuration. At  $M_\infty = 0.95$ ,  $\alpha = 15^\circ$  the computed isomach pattern is as shown in Fig. 7 and corresponding pressure distributions are shown in Fig. 8. There is

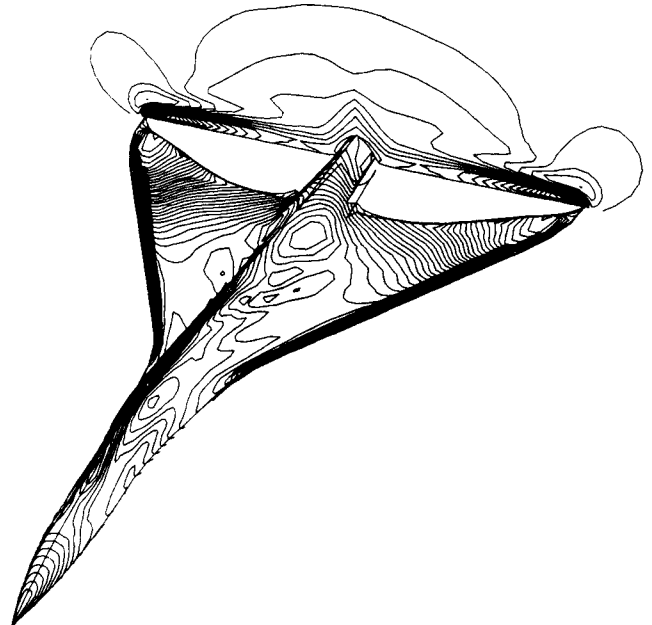


Fig. 6 Isomach Contours on Upper Wing Surface and in a Cross-sectional Plane; Configuration 1,  $M_\infty = 0.950$ ,  $\alpha = 5^\circ$

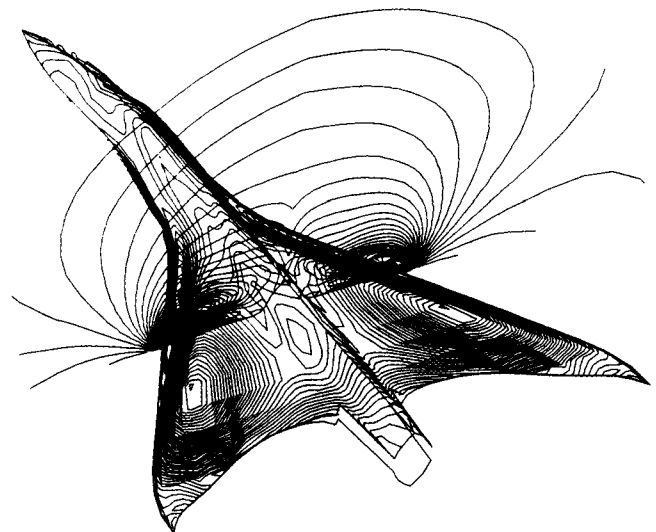


Fig. 7 Isomach Contours on Upper Wing Surface and in a Cross-sectional Plane; Configuration 1;  $M_\infty = 0.950$ ,  $\alpha = 15^\circ$

evidence of a shock along the leading edge of the configuration starting near the point where the wing first comes out. It should be mentioned that shocks are smeared over three to four mesh cells, typically. There is considerable entropy generation at these flow conditions as can be discerned in Fig. 9. The flow actually separates from the surface at the leading edge in the front

part of the wing as can be seen in Fig. 10. To be noticed in Fig. 10 are the streamlines rolling up about half-way along the wing.

Figure 11 depicts isomach contours on a second aircraft configuration at  $M_\infty = 0.80$ ,  $\alpha = 10^\circ$ . This configuration exhibits a forward-swept trailing edge and has a sharp edge at the wing and on the chine ahead of the wing. Some geometrical cross sections are visible in Fig. 12 along with the local surface pressure distributions. Computed tracks of the streamlines coming off the leading edge of the chine and the wing show that these separate from the wing, as can be seen in Fig. 13. The separation of the flow from the leading edge moves up to the chine on increasing the angle of attack to  $30^\circ$ , as Fig. 14 shows. This extensive flow separation is accompanied by large entropy production, as seen by the contours shown in Fig. 15. The corresponding isomach contours and some surface pressure distributions along the configuration are depicted in Fig. 16 and 17, respectively.

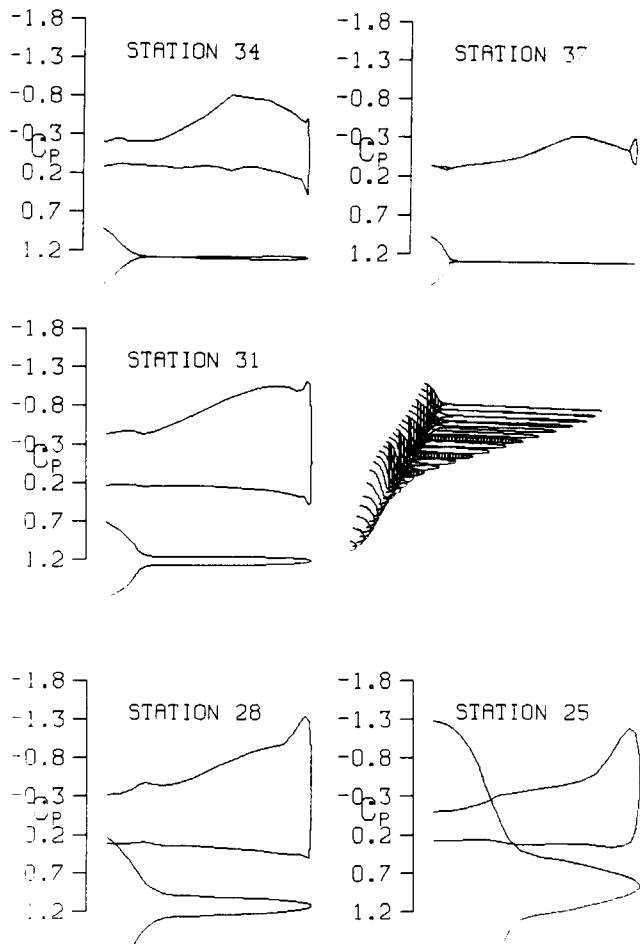
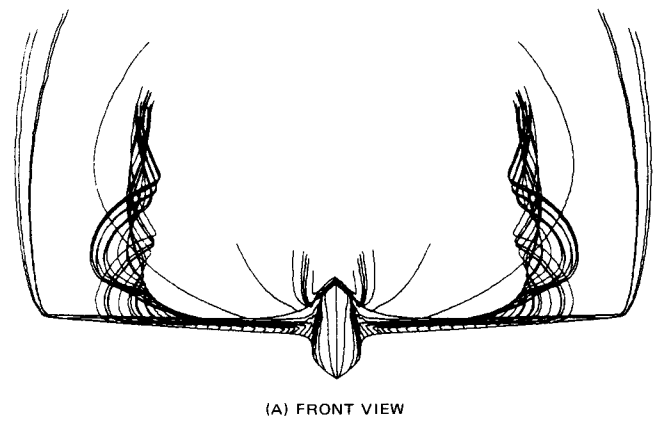


Fig. 8 Computed Surface Pressure Distributions; Configuration 1;  $M_\infty = 0.950$ ,  $\alpha = 15^\circ$



(A) FRONT VIEW

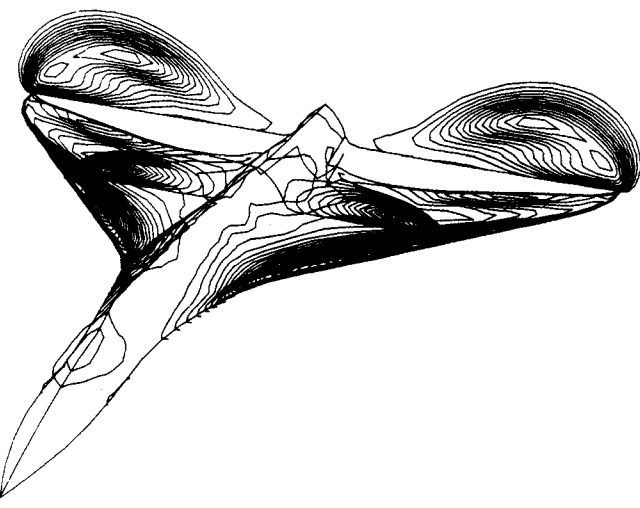


Fig. 9 Entropy Contours on Surface and in Two Cross-sectional Planes; Configuration 1;  $M_\infty = 0.950$ ,  $\alpha = 15^\circ$



(B) ISOMETRIC VIEW

Fig. 10 Streamlines from Side of the Fuselage and Leading Edge of the Wing; Configuration 1;  $M_\infty = 0.950$ ,  $\alpha = 15^\circ$

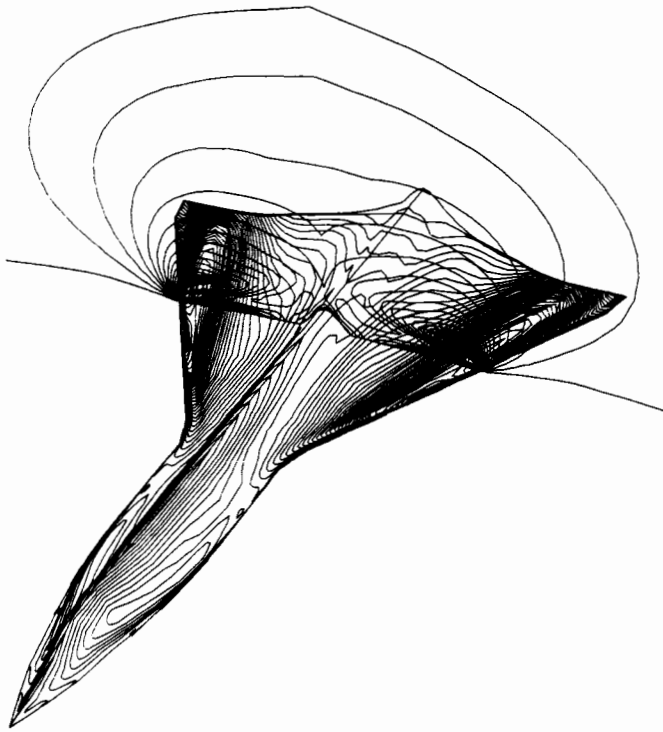
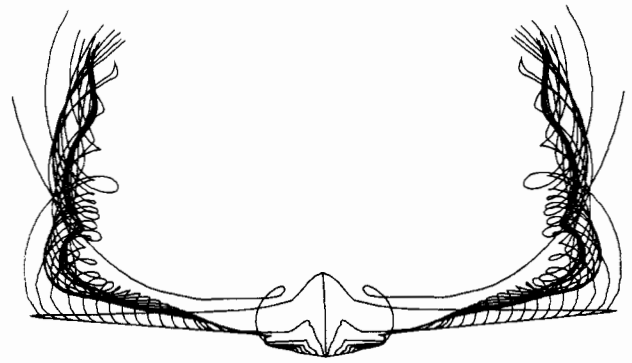
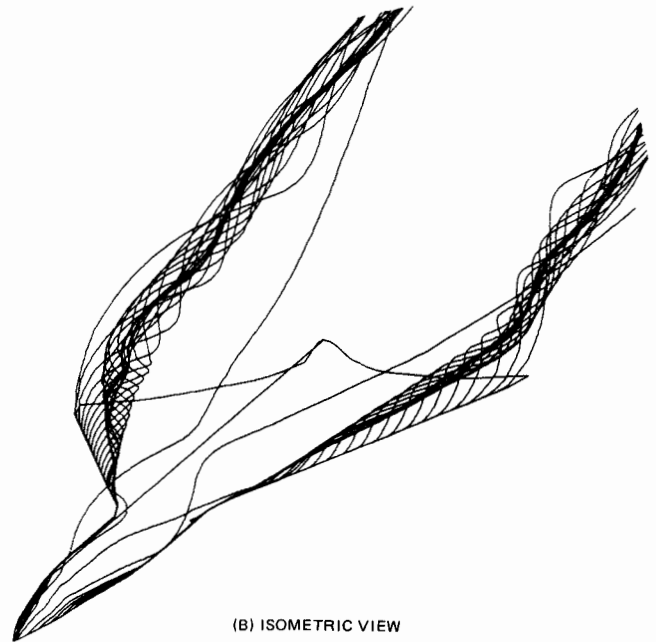


Fig. 11 Isomach Contours on Surface and in a Cross-sectional Plane; Configuration 2;  $M_\infty = 0.800$ ,  $\alpha = 10^\circ$



(A) FRONT VIEW



(B) ISOMETRIC VIEW

Fig. 13 Streamlines from Leading Edge of Chine and Wing; Configuration 2;  $M_\infty = 0.800$ ,  $\alpha = 10^\circ$

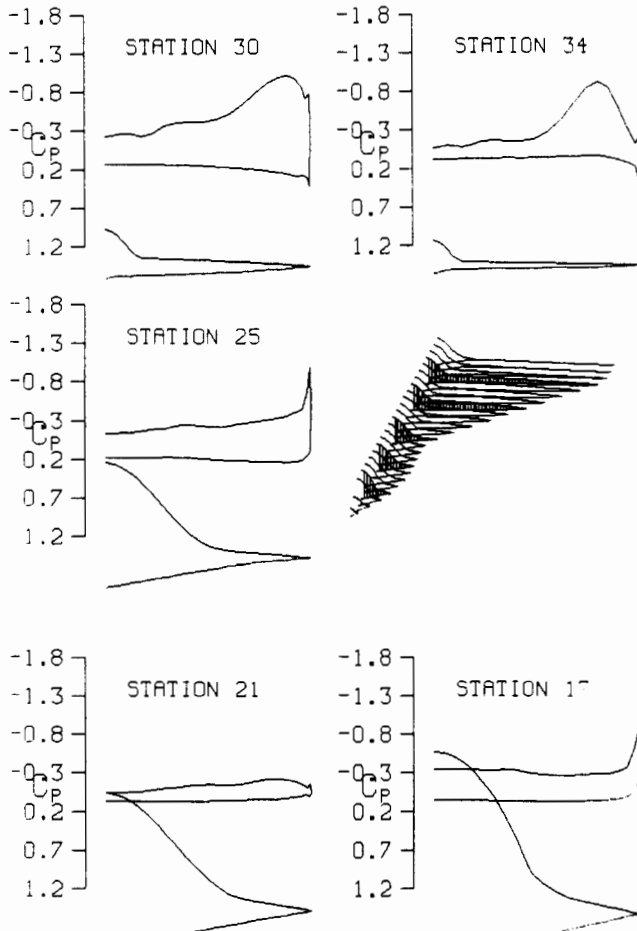
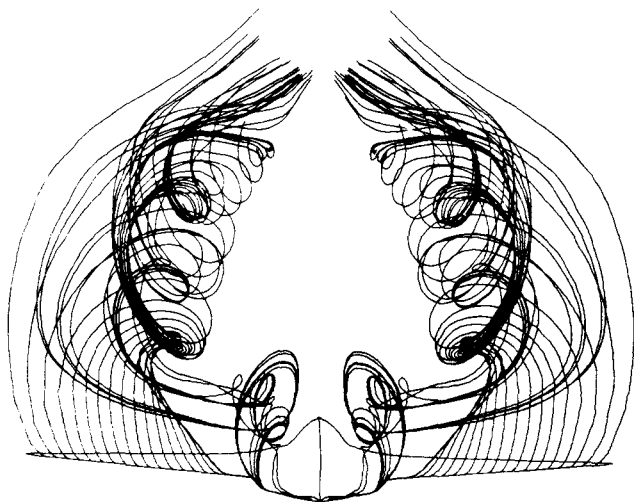
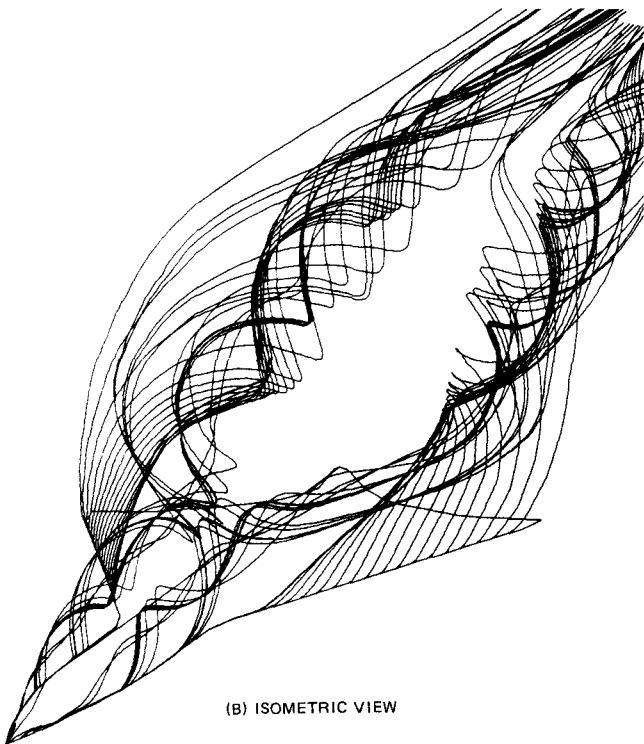


Fig. 12 Computed Surface Pressure Distributions; Configuration 2;  $M_\infty = 0.900$ ,  $\alpha = 30^\circ$

A final example in Fig. 18-21 gives results for the flow computed over this configuration at  $M_\infty = 1.50$ ,  $\alpha = 10^\circ$ . The mesh depicted in Fig. 4 was used to compute this case since with a supersonic free stream it makes a more efficient use of available grid points. In this case two-thirds of the planes in  $49 \times 49 \times 25$  mesh are distributed between the nose and tail of the aircraft with the remainder being split evenly before and aft. Isobar contours on the surface and in a vertical plane over the wing are shown in Fig. 18, and Fig. 19 gives surface pressure distributions at several stations along the aircraft. Again there is considerable entropy production as seen in Fig. 20. Flow separates at the leading edge of the chine and the streamlines coming off of it roll up tightly as they move downstream (see Fig. 21). The flow on the wing itself appears to be attached, although there seems to be a limiting line just inside the wing's leading edge.



(A) FRONT VIEW



(B) ISOMETRIC VIEW

Fig. 14 Streamlines from Leading Edge of Chine and Wing; Configuration 2;  $M_\infty = 0.800$ ,  $\alpha = 30^\circ$

#### Concluding Remarks

The new method for the calculation of steady flows over aircraft in transonic and supersonic free streams which has been described has proved to be efficient and reliable in all cases even under extreme conditions of extensive flow separation. The single-block H-O grid appears ideal for aircraft with low aspect-ratio planforms. The mesh which was used in the examples was the finest that could be handled in core on the available Cray X-MP machine. A finer mesh would be desirable to assure a dependable level of accuracy in the prediction of the aerodynamic characteristics of new configurations. The convergence rates exhibited by the multigrid time-stepping integration scheme are not very sensitive to the number of points in the

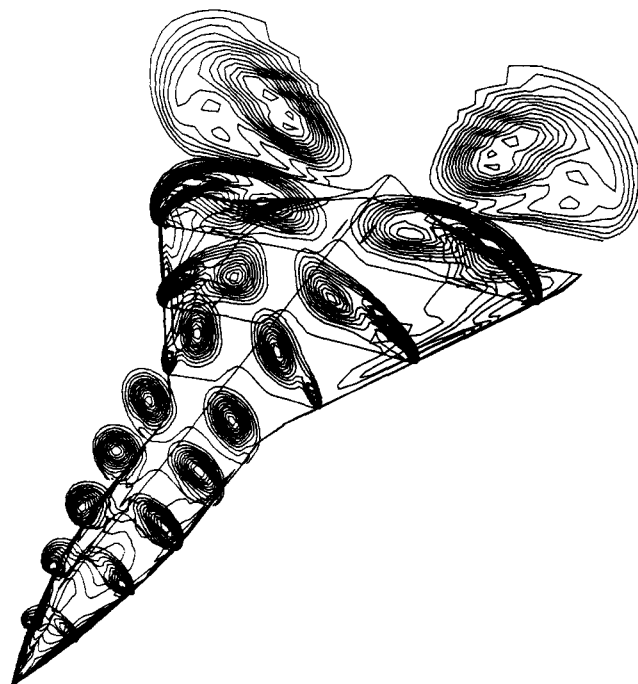


Fig. 15 Entropy Contours on Surface and in Cross-sectional Plane; Configuration 2;  $M_\infty = 0.800$ ,  $\alpha = 30^\circ$

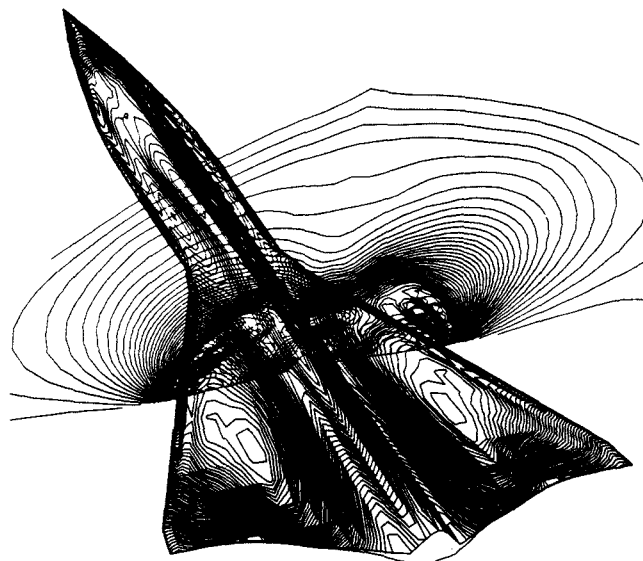


Fig. 16 Isomach Contours on Surface and in Cross-sectional Plane; Configuration 2;  $M_\infty = 0.800$ ,  $\alpha = 30^\circ$

mesh. Thus, on refinements of the mesh, one can expect the running time required to converge a particular case to increase linearly with the number of mesh points. SSD and multi-block versions of the method, which are under development, will make it possible to use finer meshes and to define adequately auxiliary lifting and control surfaces as well as engine nacelle and pods. The results obtained to date show that steady Euler flow over low aspect-ratio aircraft can now be computed quickly and cheaply enough to become part of the design process.

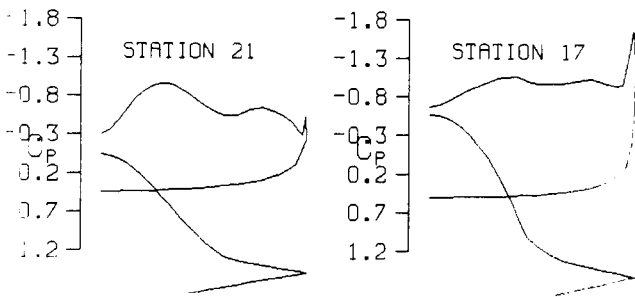
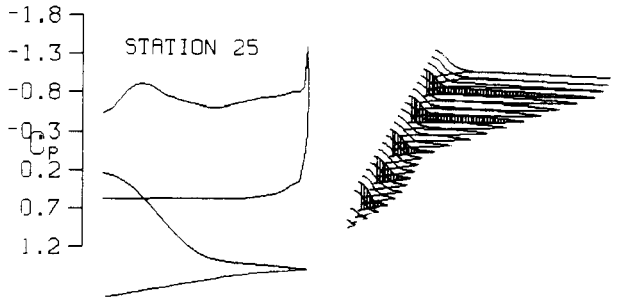
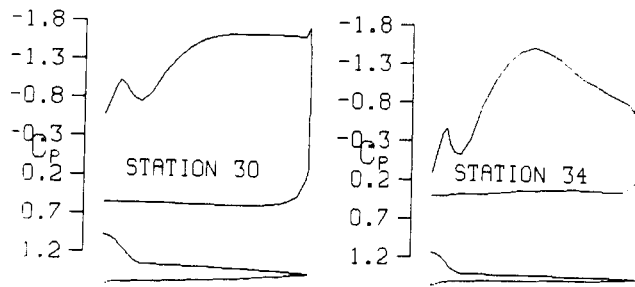


Fig. 17 Computed Pressure Distributions; Configuration 2;  $M_\infty = 0.800$ ,  $\alpha = 30^\circ$

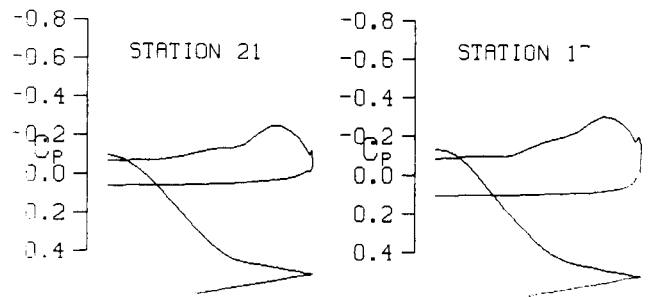
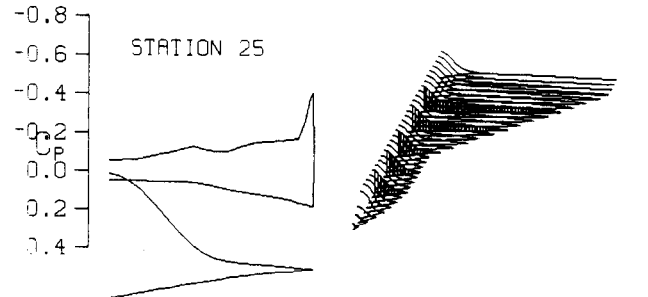
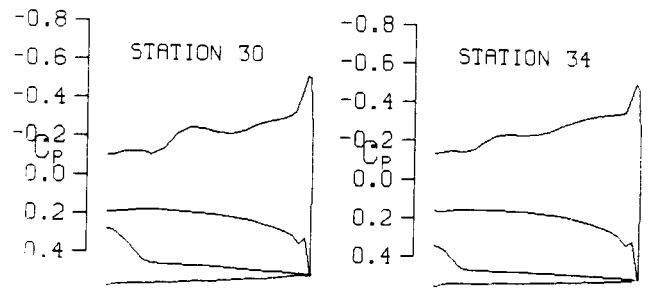


Fig. 19 Computed Pressure Distributions; Configuration 2;  $M_\infty = 1.50$ ,  $\alpha = 10^\circ$

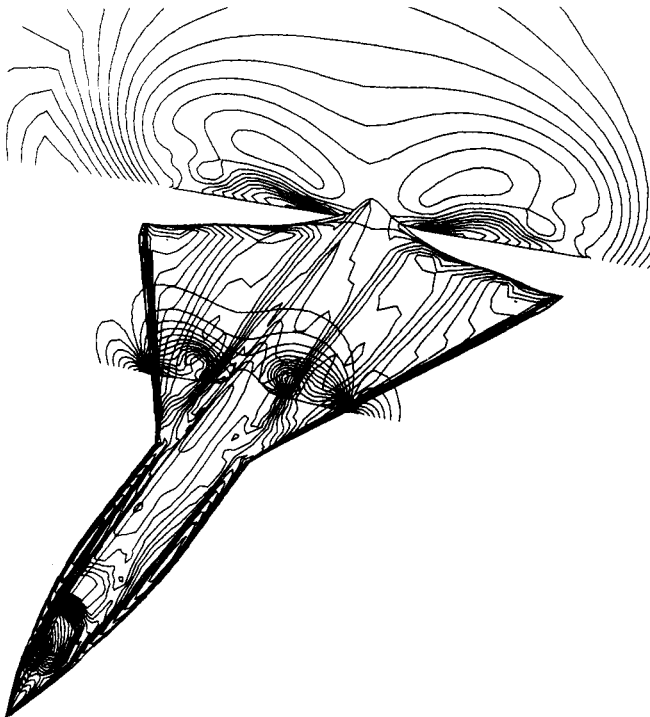


Fig. 18 Isobars on Surface and in Two Cross-sectional Planes; Configuration 2;  $M_\infty = 1.50$ ,  $\alpha = 10^\circ$

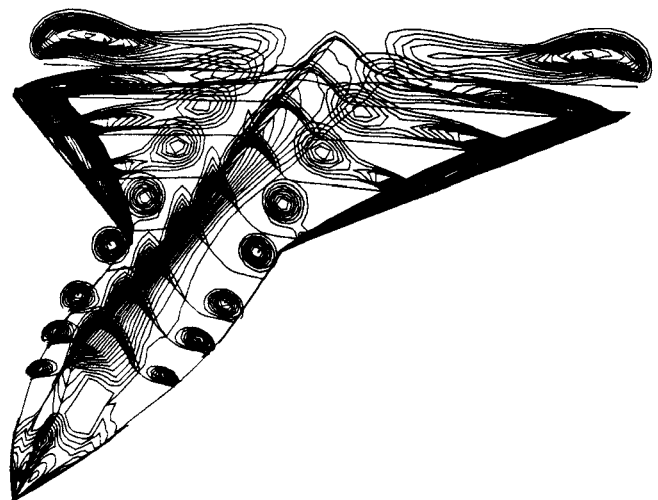
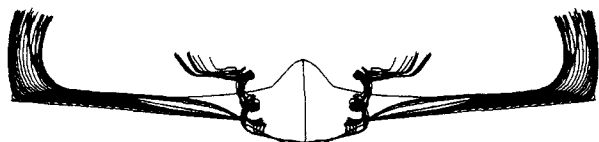
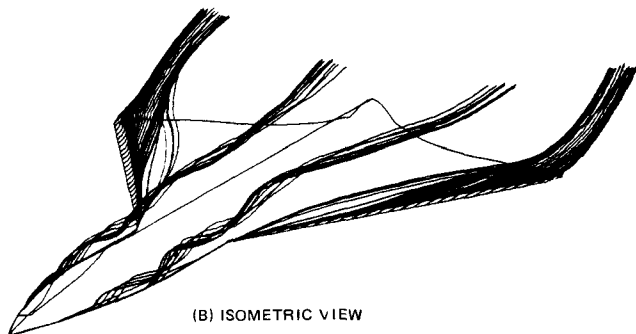


Fig. 20 Entropy Contours on Surface and in Cross-sectional Planes; Configuration 2;  $M_\infty = 1.50$ ,  $\alpha = 10^\circ$



(A) FRONT VIEW



(B) ISOMETRIC VIEW

Fig. 21 Streamlines from Leading Edge of Chine and Wing;  
Configuration 2;  $M_\infty = 1.50$ ,  $\alpha = 10^\circ$

#### References

1. Jameson, A., and Caughey, D.A., "A Finite Volume Method for Transonic Potential Flow Calculations," Proc AIAA 3rd Computational Fluid Dynamics Conf, Albuquerque, NM, 1977, pp 35-54.
2. Holst, T.L., and Thomas, S.D., "Numerical Solution of Transonic Wing Flowfields," AIAA J., Vol 18, No. 11, Nov 1980, pp 1281-1288.
3. Bristeau, M.O., Glowinski, R., Periaux, J., Perrier, P., Pironneau, O., and Poirier, G., "Transonic Flow Simulations by Finite Elements and Least Squares Methods," Proc 3rd International Conference on Finite Elements in Flow Problems, Banff, Canada, 1980, Vol 1, ed. D.H. Norrie, pp 11-29.
4. Erikson, L.L., Madson, M., and Woo, A.C., "Application of TRANAIR Full-potential Code to Complete Configurations," ICAS-86-1.3.5, 15th Congress of the Int'l Council of the Aeronautical Sciences, London, England, Sept 1986.
5. Mehta, U., and Lomax, H., "Reynolds Averaged Navier-Stokes Computations of Transonic Flows - The State of the Art," Progress in Astronautics and Aeronautics, Vol 81, Transonic Aerodynamics, 1982, ed. D. Nixon, pp 297-375.
6. McCormack, R.W., "Current Status of Numerical Solutions of the Navier-Stokes Equations," AIAA Paper 85-0032, AIAA 23rd Aerospace Sciences Mtg, Reno, NV, Jan 1986.
7. Fujii, K., and Obayashi, S., "Practical Applications of New LU-ADI Scheme for the Three-Dimensional Navier-Stokes Computation of Transonic Viscous Flows," AIAA Paper 86-0513, AIAA 24th Aerospace Sciences Mtg, Reno, NV, Jan 1986.
8. Jameson, A., Schmidt, W., and Turkel, E., "Numerical Solution of the Euler Equations by Finite Volume Methods Using Runge-Kutta Time Stepping Schemes," AIAA Paper 81-1259, AIAA 14th Fluid Dynamics and Plasma Dynamics Conf, Palo Alto, CA, 1981.
9. Ni, Ron Ho, "A Multiple Grid Scheme for Solving the Euler Equations," AIAA J., Vol 20, 1982, pp 1565-1571.
10. Jameson, A., and Baker, T., "Solution of the Euler Equations for Complex Configurations," Proc AIAA 6th Computational Fluid Dynamics Conf, Danvers, MA, 1983, pp 293-302.
11. Jameson, A., "Solution of the Euler Equations by a Multigrid Method," Applied Math and Computation, Vol 13, 1983, pp 327-356.
12. Hemker, P.W., and Spekrijse, S.P., "Multigrid Solution of the Steady Euler Equations," Proc Oberwolfach Mtg on Multigrid Methods, Dec 1984.
13. Pulliam, T.H., and Steger, J.L., "Recent Improvements in Efficiency, Accuracy and Convergence for Implicit Approximate Factorization Algorithms," AIAA Paper 85-0360, AIAA 23rd Aerospace Sciences Mtg, Reno, NV, Jan 1985.
14. Hall, M.G., "Cell Vertex Multigrid Schemes for Solution of the Euler Equations," IMA Conf on Numerical Methods for Fluid Dynamics, Reading, England, April 1985.
15. Jameson, A., and Schmidt, W., "Recent Developments in Numerical Methods for Transonic Flows," Proc 3rd Int'l Conf on Finite Elements in Nonlinear Mechanics, FENOMECH.84, Stuttgart, 1984, ed. by J. St. Doltsinis, North Holland, 1985, pp 467-493.
16. Jameson, A., Baker, T.J., and Weatherill, N.P., "Calculation of Inviscid Transonic Flow Over a Complete Aircraft," AIAA Paper 86-0103, AIAA 24th Aerospace Sciences Mtg, Reno, NV, Jan 1986.
17. Thomas, J.L., Van Leer, B., and Walters, R.W., "Implicit Flux-Split Schemes for the Euler Equations," AIAA Paper 85-1680, AIAA 18th Fluid Dynamics and Plasma Dynamics and Lasers Conf, Cincinnati, OH, July 1985.
18. Anderson, W.K., Thomas, J.L., and Whitfield, D.L., "Multigrid Acceleration of the Flux Split Euler Equations," AIAA Paper 86-0105, AIAA 24th Aerospace Sciences Mtg, Reno, NV, Jan 1986.
19. Jameson, A., "A Vertex Based Multigrid Algorithm for Three-Dimensional Compressible Flow Calculations," ASME Symp on Numerical Methods for Compressible Flow, Anaheim, CA, Dec 1986.
20. Moretti, G., "Conformal Mappings for Computations of Steady, Three-Dimensional, Supersonic Flows," Numerical/Laboratory Computer Methods in Fluid Mechanics, presented at Annual Winter Mtg of the ASME, New York, Dec 1976.

21. Siclari, M.J., "The Computational Treatment of Supersonic Wake Flows in NCOREL," AIAA Paper No. 85-0304, AIAA 23rd Aerospace Sciences Mtg, Reno, NV, Jan 1985.
22. Harten, A., "High Resolution Schemes for Hyperbolic Conservation Laws," J. Comp Phys, Vol 49, 1983, pp 357-393.
23. Jameson, A., "A Nonoscillatory Shock Capturing Scheme Using Flux Limited Dissipation," Lectures in Applied Mathematics, Vol 22, Part 1, Large Scale Computations in Fluid Mechanics, ed. by B.E. Engquist, S. Osher, and R.C.J. Somerville, A.M.S., 1985, pp 345-370.
24. Jameson, A., "Transonic Flow Calculations for Aircraft," Lecture Notes in Mathematics, Vol 1127, Numerical Methods in Fluid Dynamics, ed. by F. Brezzi, Springer-Verlag, 1985, pp 156-242.